Effects of molecular beam epitaxy growth conditions on grain size and lattice strain in *a*-axis oriented $BaSi_2$ films

Yudai Yamashita[1], Takuma Sato[1], Kaoru Toko[1], and Takashi Suemasu[1]
[1]*Institute of Applied Physics, University of Tsukuba, Tsukuba, Ibaraki 305-8573, Japan*

We grow 0.5-µm-thick *a*-axis oriented $BaSi_2$ films on Si(111) substrates by a conventional two-step growth method and compare their properties with those grown by a three-step growth method. Both grow methods consist of the initial growth of a $BaSi_2$ template layer and the following molecular beam epitaxy (MBE) to form $BaSi_2$ films. In the two-step growth method, Ba-to-Si deposition rate ratios (R_{Ba}/R_{Si}) were varied in the range 0.4–4.7 during MBE. On the other hand, in the three-step growth method, MBE-grown $BaSi_2$ layers are composed of $BaSi_2$ films grown first under Ba-rich conditions ($R_{Ba}/R_{Si} = 4.0$), followed by those grown under Si-rich conditions ($R_{Ba}/R_{Si} = 1.2$). The grain size of $BaSi_2$ films by the three-step growth method was much smaller than those grown by the two-step growth method. To our surprise, however, much higher photoresponsivity was obtained for $BaSi_2$ films grown by the three-step growth method.

* Corresponding author at:
Institute of Applied Physics, Faculty of Pure and Applied Sciences, University of Tsukuba, Tsukuba, Ibaraki 305-8573, Japan
Electronic mail: suemasu@bk.tsukuba.ac.jp

I. INTRODUCTION

Wafer-based crystalline Si solar cells account for approximately 80% of the market share, and are still the main technology.1) Thin-film solar cell materials such as chalcopyrite and cadmium telluride have also been attracting much attention because of their cost effective growth procedure and high efficiency beyond 22%.2-6) By utilizing an efficient light trapping systems, thin-film Si has also been studied for years.7-17) Under these circumstances, we have focused on semiconducting barium disilicide ($BaSi_2$)18,19) because it is composed of safe, stable, and abundant elements. Furthermore, it possesses attractive properties such as a suitable bandgap for single-junction solar cells (~1.3 eV), a high optical absorption coefficient $\alpha = 3 \times 10^4$ cm^{-3} at 1.5 eV (more than 40 times as large as that of c-Si), a large minority-carrier diffusion length $L \approx 10$ µm, and bipolar doping properties.19-24) Furthermore, $BaSi_2$ has a small lattice mismatch with Si(111), i.e., 0.1% and 1.1% along the *b*- and *c*-axis, respectively, allowing for epitaxial growth on an inexpensive Si substrate.25) For these reasons, $BaSi_2$ is considered a promising material for solar cell applications. We have achieved conversion efficiency (η) values approaching 10% in p-$BaSi_2$/n-Si heterojunction solar cells,26) which are among the highest reported for solar cells based on semiconducting silicides. Recently, we have demonstrated the operation of homojunction solar cells.27) Our final goal is to achieve operations of $BaSi_2$-pn/Ge-pn tandem solar cells. For this purpose we have also studied the epitaxial growth of $BaSi_2$ films on a Ge substrate,28) enabling us to realize flexible solar cells by using mono-like Ge films on an insulator.29)

To achieve solar cells having a high-η requires the formation of high-quality $BaSi_2$ light absorbing layers with a low defect density. Previously, we found that the Ba-to-Si deposition rate ratio (R_{Ba}/R_{Si}) during molecular beam epitaxy (MBE) has a significant impact on crystalline quality, electrical, and optical properties of $BaSi_2$ films.30,31) Defect characterizations of $BaSi_2$ have been conducted by deep level transient spectroscopy (DLTS),32) positron annihilation spectroscopy,31) Raman spectroscopy,33) and electron paramagnetic resonance,34) wherein we detected vacancy-type defects, which are considered to be Si vacancies (V_{Si}). First-principles calculations also show that V_{Si} are most likely to occur in $BaSi_2$,24) and that these vacancies give rise to localized states within the bandgap of $BaSi_2$. We have used photoresponsivity as a measure to investigate the optical properties of $BaSi_2$ films. This is because the photoresponsivity is sensitive to carrier lifetime. In our previous paper, we found that the photoresponsivity of $BaSi_2$ films grown by the two-step growth method became higher when grown at higher temperatures like 650 °C than those at 580 °C.31) Among them, for $BaSi_2$ films grown at $R_{Ba}/R_{Si} = 1.2$, namely under Si-rich conditions, the photoresponsivity reached a maximum, and decreased as R_{Ba}/R_{Si} decreased or increased from this value. This is because the density of V_{Si} in $BaSi_2$ films, which is reflected by the full-width at half maximum of the Ag mode peak by Raman spectroscopy, decreased when grown under Si-rich conditions. Furthermore, the photoresponsivity was further improved by the three-step growth method.35) However, the crystalline quality of these samples have yet to be evaluated. In this study, we compared the crystalline quality of $BaSi_2$ films grown by the two-step growth method with those by the three-step growth method, especially from the viewpoint of grain size and strain induced in $BaSi_2$ films.

II. EXPERIMENTAL METHOD

We used an ion-pumped MBE system equipped with an electron-beam evaporation source for 10N-Si and a standard Knudsen cell for 3N-Ba. We used Czochralski (CZ) n-Si(111) substrates (resistivity $\rho < 0.01$ Ωcm). The Si substrates were cleaned by RCA procedure, followed by thermal cleaning (TC) at 900 °C for 30 min in an ultra-high vacuum chamber to remove the protective oxide layer on the surface. Afterwards, we grow 0.5-µm-thick *a*-axis oriented $BaSi_2$ films on Si(111) substrates by a two-step growth method or by a three-step growth method. Both grow methods consist of the initial growth of a $BaSi_2$ template layer by deposition of Ba on a heated Si substrate by reactive deposition epitaxy (RDE) and the following MBE, that is codeposition of Ba and Si to form $BaSi_2$ films. In both cases, we first evaporated Ba onto the heated Si substrate at $T_S = 500$ °C to form a 5-nm-thick $BaSi_2$ template layer as a 1st layer by RDE. This layer acts as a seed for subsequent $BaSi_2$ layers. In the RDE process, the Ba deposition rate R_{Ba} was fixed at 1 nm/min. Then, Ba and Si were codeposited by MBE on the template to form 0.5-µm-thick *a*-axis oriented $BaSi_2$ layers at $T_S = 650$ °C. During MBE, in the two-step growth method, R_{Ba}/R_{Si} was fixed throughout the layer for each sample. R_{Si} was fixed to be 0.9 nm/min and R_{Ba} was varied from 0.3 to 4.2 nm/min to form 0.5-µm-thick $BaSi_2$ 2nd layers, giving a variation of R_{Ba}/R_{Si} from 0.4 to 4.7. On the other hand, in the three-step growth method, a 0.5-µm-thick $BaSi_2$ layer consisted of a 0.18-µm-thick $BaSi_2$ 2nd layer grown under Ba-rich conditions ($R_{Ba}/R_{Si} = 4.0$), followed by a 0.32-µm-thick $BaSi_2$ 3rd layer grown under Si-rich conditions ($R_{Ba}/R_{Si} = 1.2$). In both cases, we then formed a 3-nm-thick a-Si capping layer *in situ* at 180 °C, which acts as a surface passivation layer.36) Finally, indium-tin oxide (ITO) electrodes with a diameter of 1-mm and a thickness of 80 nm were sputtered onto the surface, and Al electrodes were formed on the entire back surface. Sample preparation details are summarized in Table 1.

The crystalline quality of the grown films was characterized by X-ray diffraction (XRD; Rigaku Smart Lab) using a Cu Kα radiation source. Out-of-plane (θ-2θ) and in-plane (φ-$2\theta_\chi$) XRD measurements were taken to determine the lattice constants using the Nelson-Riley equation.[37)] Ge crystals were used to make x-rays monochromatic. Electron backscatter diffraction (EBSD) analyses, cross-sectional transmission electron microscopy (TEM; Topcon EM-002B), reflection high-energy electron diffraction (RHEED), and x-ray diffractionanalyses have been used to characterize the crystalline quality of the grown layers. Photoresponsivity was evaluated with the use of a lock-in technique with a xenon lamp and a 25-cm-focal-length single monochromator (Bunko Keiki SM-1700A and RU-60N). The light intensity was calibrated with a pyroelectric sensor (Melles Griot 13PEM001/J). All measurement was performed at room temperature (RT).

Table I. Sample preparation details. Si substrate, values of $R_{\mathrm{Ba}}/R_{\mathrm{Si}}$ for $\mathrm{BaSi_2}$ 2nd layers by the two-step growth method, and 2nd and 3rd layers by the three-step growth method.

Sample	Si substrate	1st layer	$R_{\mathrm{Ba}}/R_{\mathrm{Si}}$ (2nd layer)	$R_{\mathrm{Ba}}/R_{\mathrm{Si}}$ (3rd layer)
A	CZ $\mathrm{n^+}$-Si(111), $\rho < 0.01\ \Omega\mathrm{cm}$	5 nm	0.4	–
B	CZ $\mathrm{n^+}$-Si(111), $\rho < 0.01\ \Omega\mathrm{cm}$	5 nm	0.9	–
C	CZ $\mathrm{n^+}$-Si(111), $\rho < 0.01\ \Omega\mathrm{cm}$	5 nm	1.2	–
D	CZ $\mathrm{n^+}$-Si(111), $\rho < 0.01\ \Omega\mathrm{cm}$	5 nm	2.3	–
E	CZ $\mathrm{n^+}$-Si(111), $\rho < 0.01\ \Omega\mathrm{cm}$	5 nm	4.7	–
F	CZ $\mathrm{n^+}$-Si(111), $\rho < 0.01\ \Omega\mathrm{cm}$	5 nm	1.2	4.0

3. Results and discussion

Figure 1(a) shows the θ-2θ XRD and RHEED patterns of $\mathrm{BaSi_2}$ films grown by the two-step growth method (samples A-E) and those by the three-step growth method (samples F). RHEED patterns were observed after the growth of $\mathrm{BaSi_2}$ films along the Si[$1\bar{1}10$] azimuth. Streaky RHEED patterns and *a*-axis oriented XRD peaks revealed that *a*-axis-oriented $\mathrm{BaSi_2}$ films were grown for samples C-F. On the other hand, with the decrease of $R_{\mathrm{Ba}}/R_{\mathrm{Si}}$, the diffraction peak intensity decreased significantly for samples A-C. Figure 1(b) shows the FWHM of $BaSi_2$ 600 peak measured by the x-ray rocking curves as a function of R_{Ba}/R_{Si}. We should note that the FHWM of sample F, grown by the three-step growth method, was as small as approximately 0.4 deg. This value is much smaller than that for sample C ($R_{Ba}/R_{Si} = 1.2$).

Figure 2 shows the internal quantum efficiency (*IQE*) spectra of sample F ($R_{Ba}/R_{Si} = 1.2 + 4.0$), grown by the three-step growth method and sample C by the two-step growth method ($R_{Ba}/R_{Si} = 1.2$) at a bias voltage of −0.1 V applied to the front ITO electrode with respect to the Al rear electrode. Sample C shows the highest *IQE* every achieved for $BaSi_2$ films by the two-step growth method.[31)] The *IQE* of sample F overcomes that of sample C and reached 90% around a wavelength of 600 nm. This value is approximately five times higher than those in sample C. To investigate the difference in crystalline quality between these samples, we performed EBSD analysis on samples A-F.

Figure 3 shows the EBSD orientation mappings of $BaSi_2$ films with various values of R_{Ba}/R_{Si}. The EBSD measurement was carried out at intervals of 80 nm. Figures 3(a) – 3(f) are EBSD images taken in the transverse direction (TD), and Figs. 3(g) – 3(l) are those in the normal direction (ND) with respect to the sample surface. We see three colors represented by red, blue, and green in the TD images, indicating that there are three crystal variants of *a*-axis oriented $BaSi_2$ films on Si(111).[38)] The crystal grain size increased from 0.1 μm to several μm as the R_{Ba}/R_{Si} increased, namely when grown under Ba-rich conditions. Among these samples, the photoresponsivity reached a maximum at $R_{Ba}/R_{Si} = 1.2$.[31)] Regarding sample F, grown by the three-step growth method ($R_{Ba}/R_{Si} = 4.0$, followed by 1.2), however, the crystal orientation normal to sample plane was not identified for almost half the area as shown in Fig. 3(I). In the EBSD analyses, Kikuchi patterns are used to determine the crystal orientation. It is therefore difficult to determine the crystal orientation when crystalline grains are small, and there are more than one grains within the spot size of the electron beam, and thus multiple Kikuchi patterns exist. Small grains of $BaSi_2$ were observed in the TEM image of sample F as discussed next.

We performed TEM observations on sample F. Figures 5(a) – 5(c) are the bright-field (BF) TEM image, the dark-field (DF) TEM image, and the selected area electron diffraction (SAED) pattern taken from the region of the $BaSi_2$ layers, respectively. We can see that grain boundaries (GBs) of $BaSi_2$ extend straight and perpendicular to the Si substrate. The horizontal grain size is approximately 0.2 μm or smaller. These *a*-axis-oriented $BaSi_2$ films possess three crystal variants rotated around the surface normal at 120° with respect to one another.[19)] In Fig.

5(b), brighter regions are one of the three crystal variants, showing that small grains are also aligned laterally the same as larger grains. In general, GBs act not only as recombination centers but also diffusion paths for impurity atoms.[39,40] On the other hand, in *a*-axis oriented $BaSi_2$ epitaxial films, the GBs do not behave as recombination centers from viewpoints of experiment[41] and first-principle calculation.[42] The experimental results show that there are much more GBs in sample F than in sample C from Fig. 3, but $BaSi_2$ films in sample F shows higher photoresponsivity in Fig. 2. This means that the GBs in sample F do not work as recombination centers like in *a*-axis oriented epitaxial films.

We next discuss the influence of the reduction of the grain size of $BaSi_2$ by the three-stage growth method. Figure 6 shows lattice constants a, b, c and volume V of $BaSi_2$ films for samples A-F. Both the out-of-plane and in-plane lattice constants were calculated from the peak positions in the θ-2θ and φ-$2\theta_\chi$ XRD patterns, respectively. Measurement errors were minimized by using the Nelson-Riley equation for the calculation.[37] Lattice constants b and c increased for $BaSi_2$ films grown under Si-rich conditions, meaning the expansion of the lattice occurs in the in-plane direction. On the other hands, all the lattice constants decreased significantly for sample F, grown by the three-step growth method, compared to those by the two-step growth method, and V decreased accordingly. This volume is smaller than that of bulk $BaSi_2$.[18] Those results mean that the $BaSi_2$ lattice is under a compressive strain in both the perpendicular and the in-plane directions in sample F. We therefore speculate that the grain size of $BaSi_2$ films decreased to mitigate the stress contained in the film. We recently explored a possibility to manipulate the energy band structure of $BaSi_2$ by changing a, b, and c lattice parameters,[43] wherein the band gap reduction occurs by *ab initio* calculations when one of the lattice parameters decreases while the other two are kept constant. However, we did not anticipate what happens when all the lattice parameters a, b, and c decrease like in sample F. Therefore, we investigate the absorption edge of sample F. For this purpose, we derived the absorption edge of $BaSi_2$ films in samples C and F. The generation rate G of electron-hole pairs per unit time and volume at a distance x from the surface of $BaSi_2$ is described by

$$G \propto \alpha \frac{P_{\mathrm{opt}}}{\hbar\omega} \exp(-\alpha x), \qquad (1)$$

where P_{opt} is the incident optical power per unit area, α is the optical absorption coefficient, and $\hbar\omega$ is the photon energy. The photocurrent I_{p} is proportional to G. Since α is small around the band edge, exp $(-\alpha x)$ in Eq. (1) is much less dependent on phonon energy. Thus, the photocurrent per incident photon, $I_{\mathrm{p}}/(P_{\mathrm{opt}}/\hbar\omega)$, is likely to be proportional to α.

Figures 7(a) and 7(b) show plots of $[I_\mathrm{p}/(P_\mathrm{opt}/\square\omega)]^{1/2}$ and $[I_\mathrm{p}/(P_\mathrm{opt}/\square\omega)]^2$ vs $\square\omega$ for a bias voltage of −0.1 V for $BaSi_2$ of sample C ($R_\mathrm{Ba}/R_\mathrm{Si} = 1.2$), and F ($R_\mathrm{Ba}/R_\mathrm{Si} = 4.0$, followed by 1.2), respectively. In the lower-energy region, the $[I_\mathrm{p}/(P_\mathrm{opt}/\square\omega)]^{1/2}$ vs $\square\mathrm{\omega}$ plot is linear. Each indirect absorption edge is derived to be approximately 1.176 and 1.237 eV, respectively, from the intersection of straight line with the abscissa. Furthermore, in the higher-energy region, the $[I_\mathrm{p}/(P_\mathrm{opt}/\square\omega)]^2$ vs $\square\omega$ plot can be well approximated by a straight line, resulting in a direct absorption edge of approximately 1.388 and 1.412 eV, respectively. Therefore, the absorption edge of $BaSi_2$ formed by the three-step method is larger than that of $BaSi_2$ films grown by Si-rich conditions, suggesting that it was caused by compressive strain. These results indicate that much further expansion of E_g in *a*-axis oriented $BaSi_2$ films can be anticipated by controlling the degree of compressive strain.

IV. CONCLUSION

We fabricated 0.5-μm-thick *a*-axis oriented $BaSi_2$ films at 650 °C by MBE using the three-step growth method and compared their crystalline quality and optical properties with those grown by the two-step growth method. EBSD and TEM observations showed that the grain size of $BaSi_2$ films significantly decreased from several μm to 0.1 μm as the $R_\mathrm{Ba}/R_\mathrm{Si}$ decreased, and that of $BaSi_2$ films grown by the three-step growth techniques was also approximately 0.1 μm. The $BaSi_2$ films grown by the three-step growth method showed higher *IQE*s by approximately five times than those by the two-step growth method; it reached 90% at a bias voltage of –0.1 V to the ITO front electrode with respect to the Al rear electrode. XRD measurement showed that the $BaSi_2$ films were under compressive strains in in the *a*-, *b*-, and *c*-axis directions. The absorption edge of $BaSi_2$ grown by the three-step method was expanded compared to $BaSi_2$ films grown by the two-step growth method. This is probably caused by the compressive strain in $BaSi_2$ films.

ACKNOWLEDGEMENTS

This work was financially supported by JSPS KAKENHI Grant Numbers 17K18865 and 18H03767 and JST MIRAI. One of the authors (Y.Y.) was financially supported by a Grant-in-Aid for JSPS Fellows (19J21372).

Reference

1) K. Yoshikawa, H. Kawasaki, W. Yoshida, K. Konishi, K. Nakano, T. Uto, D. Adachi, M. Kakematsu, H. Uzu, and K. Yamamoto, Nat. Energy **2**, 17032 (2017).

2) I. Repins, M. A. Contreras, B. Egaas, C. DeHart, J. Scharf, C. L. Perkins, B. To, and R. Noufi, Prog. Photovoltaics **16**, 235 (2008).

3) H. Katagiri, K. Jimbo, W. S. Maw, K. Oishi, M. Yamazaki, H. Araki, and A. Takeuchi, Thin Solid Films **517**, 2455 (2009).

4) P. Jackson, R. Wuerz, D. Hariskos, E. Lotter, W. Witte, and M. Powalla, Phys. Status Solidi Rapid Research Lett. **10**, 583 (2016).

5) J. M. Burst, J. N. Duenow, D. S. Albin, E. Colegrove, M. O. Reese, J. A. Aguiar, C. S. Jiang, M. K. Patel, M. M. Al-Jassim, and D. Kuciauskas, Nat. Energy **1**, 16015 (2016).

6) S. G. Kumar, and K. S. R. K. Rao, Energy & Environmental Sci. 7, **45** (2014).

7) R. G. Gordon, J. Proscia, F. B. Ellis, Jr., and A. E. Delahoy, Sol. Energy Mater. **18**, 263 (1989).

8) P. Campbell, Sol. Energy Mater. **21**, 165 (1990).

9) H. Sasaki, H. Morikawa, Y. Matsuno, M. Deguchi, T. Ishihara, H. Kumabe, T. Murotani, and S. Mitsui, Jpn. J. Appl. Phys. **33**, 3389 (1994).

10) J. Meier, S. Dubail, R. Platz, P. Torres, U. Kroll, J. A. A. Selvan, N. P. Vaucher, Ch. Hof, D. Fischer, H. Keppner, R. Flückiger, A. Shah, V. Shklover, and K.-D. Ufert, Sol. Energy Mater. Sol. Cells **49**, 35 (1997).

11) O. Vetterl, F. Finger, R. Carius, P. Hapke, L. Houben, O. Kluth, A. Lambertz, A. Mück, B. Rech, and H. Wagner, Sol. Energy Mater. Sol. Cells **62**, 97 (2000).

12) A. Poruba, A. Fejfar, Z. Remes, J. Springer, M. Vanecek, and J. Kocka, J. Appl. Phys. **88**, 148 (2000).

13) J. Müller, B. Rech, J. Springer, and M. Vanecek, Sol. Energy **77**, 917 (2004).

14) M. Berginski, J. Hüpkes, M. Schulte, G. Schöpe, H. Stiebig, and B. Rech, J. Appl. Phys. **101**, 074903 (2007).

15) D. Zhou and R. Biswas, J. Appl. Phys. **103**, 093102 (2008).

16) A. Hongsingthong, T. Krajangsang, I. A. Yunaz, S. Miyajima, and M. Konagai, Appl. Phys. Express **3**, 051102 (2010).

17) H. Sai, Y. Kanamori, and M. Kondo, Appl. Phys. Lett. **98**, 113502 (2011).

18) M. Imai and T. Hirano, J. Alloys Compd. **224**, 111 (1995).

19) T. Suemasu and N. Usami, J. Phys. D **50**, 023001 (2017).

20) K. Toh, T. Saito, and T. Suemasu, Jpn. J. Appl. Phys. **50**, 068001 (2011).

21) D. B. Migas, V. L. Shaposhnikov, and V. E. Borisenko, Phys. Status Solidi B **244**, 2611 (2007).

22) M. Kumar, N. Umezawa, and M. Imai, J. Appl. Phys. **115**, 203718 (2014).

23) M. Kumar, N. Umezawa, and M. Imai, Appl. Phys. Express **7**, 071203 (2014).

24) M. Kumar, N. Umezawa, W. Zhou, and M. Imai, J. Mater. Chem. A **5**, 25293 (2017).

25) R. A. McKee and F. J. Walker, Appl. Phys. Lett. **63**, 2818 (1993).

26) T. Deng, T. Sato, Z. Xu, R. Takabe, S. Yachi, Y. Yamashita, K. Toko, and T. Suemasu, Appl. Phys. Express **11**, 6 (2018).

27) K. Kodama, Y. Yamashita, K. Toko, and T. Suemasu, Appl. Phys. Express **12**, 041005 (2019).

28) R. Takabe, S. Yachi, D. Tsukahara, K. Toko, and T. Suemasu, Jpn. J. Appl. Phys. **56**, 05DB02 (2017).

29) K. Toko, R. Yoshimine, K. Moto, and T. Suemasu, Sci. Rep. **7**, 16981 (2017).

30) R. Takabe, T. Deng, K. Kodama, Y. Yamashita, T. Sato, K. Toko, and T. Suemasu, J. Appl. Phys. **123**, 045703 (2018).

31) Y. Yamashita, Y. Takahara, T. Sato, K. Toko, A. Uedono, and T. Suemasu, Appl. Phys. Express **12**, 055506 (2019).

32) Y. Yamashita, T. Sato, M. Emha Bayu, Kaoru Toko, T. Suemasu, Jpn. J. Appl. Phys. **57**, 075801 (2018).

33) T. Sato, H. Hoshida, R. Takabe, K. Toko, Y. Terai, and T. Suemasu, J. Appl. Phys. **124**, 025301 (2018).

34) T. Sato, C. Lombard, Y. Yamashita, Z. Xu, L. Benincasa, K. Toko, a nd T. Suemasu, Appl. Phys. Express **12**, 061005 (2018).

35) Y. Yamashita, T. Sato, N. Saitoh, N. Yoshizawa, K. Toko, T. Suemasu, J. Appl. Phys. **126**, 215301 (2019).

36) R. Takabe, H. Takeuchi, W. Du, K. Ito, K. Toko, S. Ueda, A. Kimura, and T. Suemasu, J. Appl. Phys. **119**, 165304 (2016).

37) J. B. Nelson, D. P. Riley, Proc. Phys. Soc. **57**, 160 (1945).

38) R. Takabe, K. Nakamura, M. Baba, W. Du, M. A. Khan, K. Toko, M. Sasase, K. O. Hara, N. Usami, and T. Suemasu, Jpn. J. Appl. Phys. **53**, 04ER04 (2014).

39) M. Matsuda, J. Nowotny, Z. Zhang, C. C. Sorrell, Solid State Ionics **111**, 301 (1998).

40) I. V. Belova, T. Fiedler, N. Kulkarni, and G. E. Murch, Phlos. Mag. **92**, 1748 (2012).

41) R. Takabe, K. O. Hara, M. Baba, W. Du, N. Shimada, K. Toko, N. Usami, and T. Suemasu, J. Appl. Phys. **115**, 193510 (2014).

42) M. Baba, M. Kohyama, and T. Suemasu, J. Appl. Phys. **120**, 085311 (2016).

43) D. A Shohonov, D. B. Migas, A. B. Filonov, and V. E. Borisenko, K. Takabe, and T. Suemasu, Thin Solid Films **686**, 137436 (2019).

Fig. 1 (a) θ-2θ XRD pattern of $BaSi_2$ films grown by the two-step growth technique (samples A-E) and those by the three-step growth technique (samples F). RHEED patterns were observed after the growth of $BaSi_2$ films along the Si$[1\bar{1}10]$ azimuth. (b) FWHM of the x-ray rocking curve of the $BaSi_2$ 600 peak intensity as a function of R_{Ba}/R_{Si}.

Fig. 2 *IQE* spectra of samples C and F at a bias voltage of –0.1 V applied to the front ITO electrode with respect to the backside Al electrode.

Fig. 3 EBSD crystal orientation maps of (a) – (e) TD images and (g) – (k) ND images of $BaSi_2$ grown by the two-step growth method under several values of R_{Ba}/R_{Si}. (f) and (l) are those for sample F, grown by the three-step growth method.

Fig. 4 Cross-sectional TEM characterization of sample F, $BaSi_2$ films grown by the three-step growth technique. (a) Bright-field TEM image. (b) Dark-field TEM image using the $BaSi_2\{010\}$ plane reflection. (c) SAED pattern taken from the region including $BaSi_2$ layers.

Fig. 5 Dependence of lattice constant (a) a, (b) b, (c) c and (d) lattice volume V on R_{Ba}/R_{Si}.

Fig. 6 Dependence of the square root and square of the photocurrent per incident photon on photon energy for $BaSi_2$. A bias voltage of −0.1 V was applied to the front ITO electrode with respect to the bottom Al electrode to extract photogenerated holes to the ITO electrode.

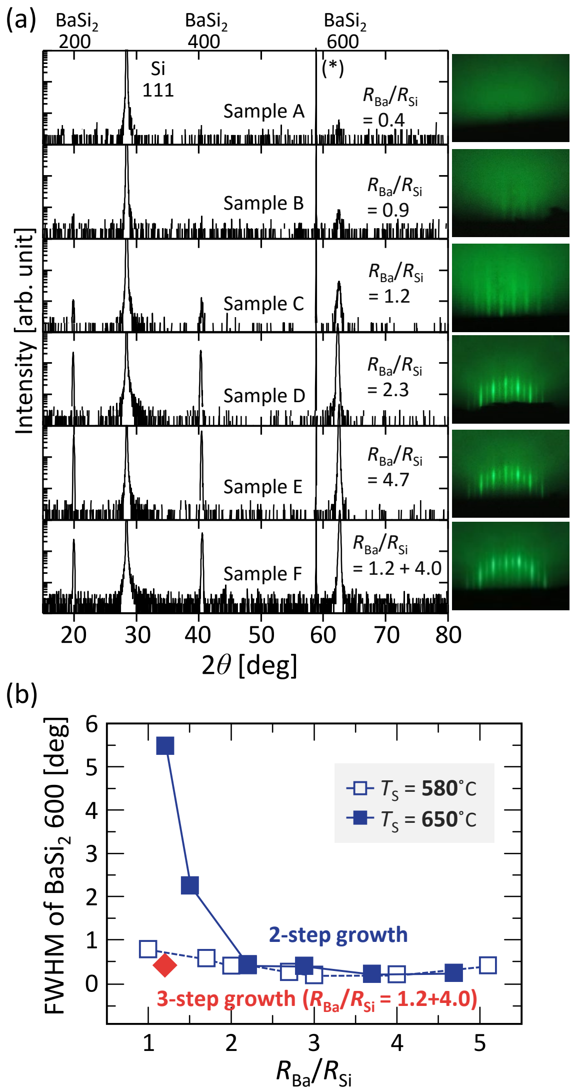
(a)
BaSi2 200
BaSi2 400
BaSi2 600
Si 111
(*)
Sample A
RBa/RSi = 0.4
Sample B
RBa/RSi = 0.9
Sample C
RBa/RSi = 1.2
Sample D
RBa/RSi = 2.3
Sample E
RBa/RSi = 4.7
Sample F
RBa/RSi = 1.2 + 4.0
Intensity [arb. unit]
20 30 40 50 60 70 80
2θ [deg]
(b)
FWHM of BaSi2 600 [deg]
6 5 4 3 2 1 0
TS = 580°C
TS = 650°C
2-step growth
3-step growth (RBa/RSi = 1.2+4.0)
1 2 3 4 5
RBa/RSi

Fig. 1

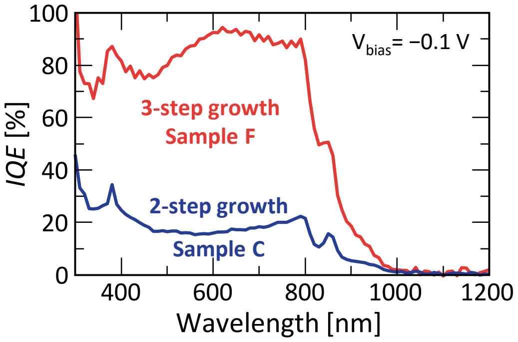
100
80
60
40
20
0
IQE [%]
400
600
800
1000
1200
Wavelength [nm]
V_{bias}= −0.1 V
3-step growth
Sample F
2-step growth
Sample C

Fig. 2

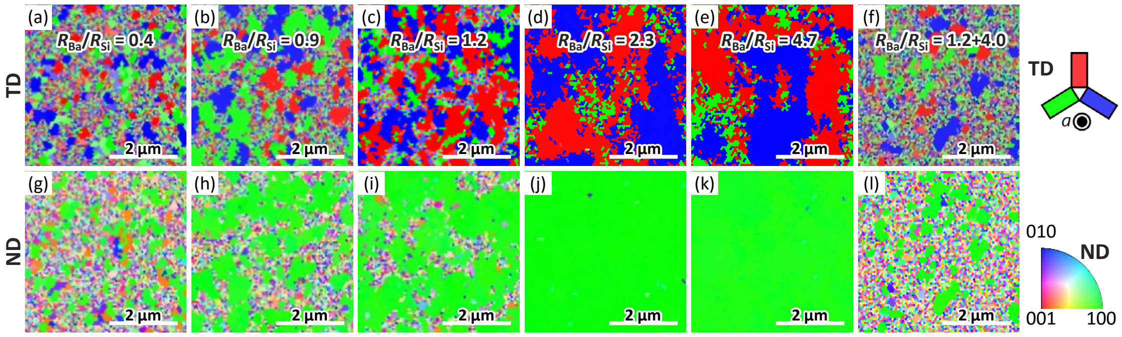
(a)
R_Ba/R_Si = 0.4
(b)
R_Ba/R_Si = 0.9
(c)
R_Ba/R_Si = 1.2
(d)
R_Ba/R_Si = 2.3
(e)
R_Ba/R_Si = 4.7
(f)
R_Ba/R_Si = 1.2+4.0
TD
TD
a
(g)
(h)
(i)
(j)
(k)
(l)
ND
ND
010
001
100
2 µm

Fig. 3

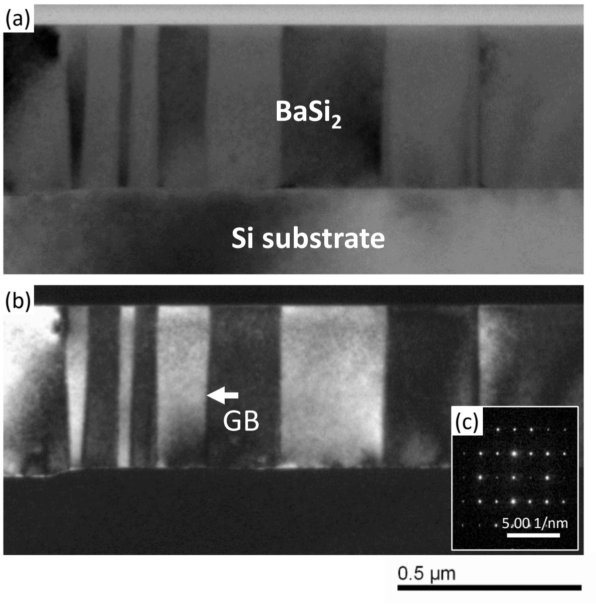

Fig. 4

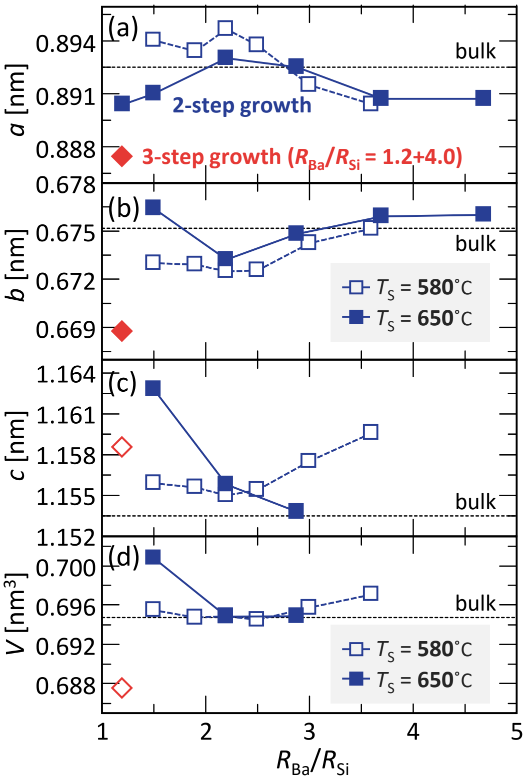
(a)
0.894
0.891
0.888
a [nm]
bulk
2-step growth
3-step growth (R_{Ba}/R_{Si} = 1.2+4.0)
0.678
(b)
0.675
0.672
0.669
b [nm]
bulk
T_S = 580°C
T_S = 650°C
1.164
(c)
1.161
1.158
1.155
1.152
c [nm]
bulk
(d)
0.700
0.696
0.692
0.688
V [nm^3]
bulk
T_S = 580°C
T_S = 650°C
1
2
3
4
5
R_{Ba}/R_{Si}

Fig. 5

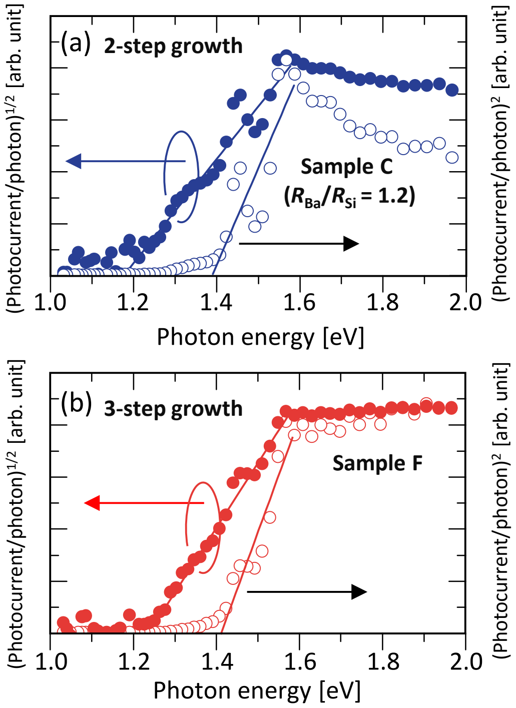
(a) 2-step growth
Sample C
(R_{Ba}/R_{Si} = 1.2)
(Photocurrent/photon)$^{1/2}$ [arb. unit]
(Photocurrent/photon)^2 [arb. unit]
1.0
1.2
1.4
1.6
1.8
2.0
Photon energy [eV]
(b) 3-step growth
Sample F
(Photocurrent/photon)$^{1/2}$ [arb. unit]
(Photocurrent/photon)^2 [arb. unit]
1.0
1.2
1.4
1.6
1.8
2.0
Photon energy [eV]

Fig. 6